Full Length Article

# van der Waals epitaxy of SnS film on single crystal graphene buffer layer on amorphous SiO$_2$/Si

Yu Xiang [a,b,*], Yunbo Yang [a,b], Fawen Guo [a,b], Xin Sun [a,b], Zonghuan Lu [a,b], Dibyajyoti Mohanty [a,c], Ishwara Bhat [a,c], Morris Washington [a,b], Toh-Ming Lu [a,b], Gwo-Ching Wang [a,b]

[a] Center for Materials, Devices, and Integrated Systems, Rensselaer Polytechnic Institute, 110, 8thStreet, Troy, NY 12180-3950, USA
[b] Department of Physics, Applied Physics and Astronomy, Rensselaer Polytechnic Institute, 110, 8thStreet, Troy, NY 12180-3950, USA
[c] Department of Electrical, Computer and Systems Engineering, Rensselaer Polytechnic Institute, 110, 8thStreet, Troy, NY 12180-3950, USA

## ARTICLE INFO

## ABSTRACT

Conventional hetero-epitaxial films are typically grown on lattice and symmetry matched single crystal substrates. We demonstrated the epitaxial growth of orthorhombic SnS film (∼500 nm thick) on single crystal, monolayer graphene that was transferred on the amorphous SiO$_2$/Si substrate. Using X-ray pole figure analysis we examined the structure, quality and epitaxy relationship of the SnS film grown on the single crystal graphene and compared it with the SnS film grown on commercial polycrystalline graphene. We showed that the SnS films grown on both single crystal and polycrystalline graphene have two sets of orientation domains. However, the crystallinity and grain size of the SnS film improve when grown on the single crystal graphene. Reflection high-energy electron diffraction measurements show that the near surface texture has more phases as compared with that of the entire film. The surface texture of a film will influence the growth and quality of film grown on top of it as well as the interface formed. Our result offers an alternative approach to grow a hetero-epitaxial film on an amorphous substrate through a single crystal graphene buffer layer. This strategy of growing high quality epitaxial thin film has potential applications in optoelectronics.

© 2017 Elsevier B.V. All rights reserved.

## 1. Introduction

Tin mono-sulfide (SnS) has drawn interests among photovoltaic cells (PVCs) research community worldwide [1,2]. The advantages of SnS film include an optical energy band gap of 1.3 eV which is close to the optimum value required for efficient light absorption, a high optical absorption coefficient of >10$^4$ cm$^{-1}$ above the photon energy threshold (∼1.3 eV) [3], low cost, and non-toxic. SnS also has other applications in photodetectors [4], gas sensors [5], and Li-ion batteries [6]. One of the major challenges in the SnS thin film based PVCs is producing high quality materials [7]. Attempts have been made to grow high quality epitaxial SnS film by using lattice-matched (LM) single crystal substrates such as MgO(001) [8] and Al(100) [9]. In this conventional hetero-epitaxy the lattice mismatch and thermal mismatch between the chosen overlayer and the substrate materials are usually small. The large lattice mismatch

and strong chemical bonds at the interface may have several consequences: (1) Strain develops at the interface. (2) Various structural defects may nucleate in the overlayer. (3) The chemical inhomogeneity may be introduced in the overlayer. (4) The intermixing between the overlayer and substrate may occur at the interface. If the dangling bonds on a substrate are not fully passivated, the surface reconstruction and lattice relaxation could happen. This could affect the growth mode and structural quality of an overlayer grown on it later.

Limited choices of LM single crystal substrates, possible structural imperfect overlayer, and chemical bondings at the interface of the hetero-junction in conventional hetero-epitaxy led researchers to pursue alternative routes to grow high quality epitaxial SnS film. Apart from being a promising light absorption material, SnS also belongs to a class of materials called layered metal chalcogenide (LMC). The LMC materials have rich fundamental physical and chemical properties and potential applications in electronics and optoelectronics, which has stimulated intense research activities world-wide in recent years [10]. A LMC material consists of a stacking of two-dimensional (2D) MXs layers where M is a metal

from groups IV, V or VI and X is a chalcogen atom from S, Se or Te. A unique characteristic of this class of materials is that the chalcogenide atoms are chemically saturated and, as a result, the weak inter-layer interactions are dominated by the van der Waals force [11]. The van der Waals force nature of the interaction between SnS layers makes it possible to grow van der Waals epitaxies (vdWEs) [12]. Compared to conventional hetero-epitaxies, the van der Waals substrate may not give rise to large strain in the overlayer, and therefore high density structural and chemical defects may not develop in the overlayer and at the interface [13]. Thus, the lattices between the overlayer and the substrate could have a large mismatch and the overlayer could be incommensurate with the substrate at the interface [14]. The lift of this restriction on lattice match greatly broadens the choices of materials used in heteroepitaxy systems. One can imagine the growth of either layer [15] or even non-layer [16–18] epitaxial films or non-planar nanostructures [19] on the van der Waals substrates such as graphene.

All these merits of vdWEs make it a very favorable method to grow high-quality SnS film. SnS film has been successfully grown on transferred double-layer, polycrystalline graphene buffer layer on single crystal GaAs(100) or amorphous $SiO_2$/Si substrates [15,20]. The double-layer, polycrystalline graphene was grown by chemical vapor deposition (CVD). These previous reports indicate that the SnS films grown on transferred double-layer, polycrystalline graphene on an amorphous substrate or a GaAs(100) substrate have narrower rocking curves and stronger out-of-plane orientations compared with that on substrates without the transferred double graphene layer. However, the in-plane epitaxy appears to contain many orientation domains.

In this work, we report the growth and characterization of high-quality SnS ($\sim$500 nm thick) films using thermal evaporation of SnS powders onto the homemade single crystal graphene which has one orientation domain and polycrystalline commercial graphene which has two dominant orientation domains with 30° rotation relative to each other. We will refer to these two substrates as the single crystal graphene and the polycrystalline graphene in the following text. We characterized the morphology and surface roughness of graphene and SnS film using atomic force microscopy (AFM) and scanning electron microscopy (SEM). The grain size and misorientation were measured by electron backscatter diffraction (EBSD). The graphene symmetry and number of orientation domains were examined by reflection high energy electron diffraction (RHEED) 2D reciprocal space mapping. The structure and texture of the bulk SnS films were measured by X-ray diffraction (XRD) and X-ray pole figure. For structure and texture near the film surface, RHEED was used. The in-plane epitaxial relationship at the interface of SnS and graphene was determined by combing XRD and RHEED. The vibrational and electrical properties of the films were measured by Raman spectroscopy and Hall measurement, respectively.

## 2. Experimental

### 2.1. Buffered substrates

#### 2.1.1. Commercial polycrystalline graphene

The polycrystalline graphene buffered $SiO_2$/Si substrate used in our experiment was a commercial product (graphene-supermarket.com). Monolayer, polycrystalline graphene on 1 cm × 1 cm silicon wafer (p-doped) with <100> orientation and a silicon oxide coating ($\sim$150 nm) was prepared by the company following the procedure developed by Li et al. [21]. and then transferred onto the silicon wafer using the "PMMA-mediated" approach [22,23]. 95% of the surface area is covered with monolayer graphene, while 10–30% of this area is also covered with bilayer graphene islands. Prior to the SnS film deposition the morphology and grain orientations of this commercial graphene substrate were characterized by using SEM, AFM, and RHEED. See figures later.

#### 2.1.2. Homemade single crystal graphene

The homemade graphene was first epitaxially grown on single-crystalline Cu(111)/sapphire substrates with a low pressure chemical vapor deposition method. The single-crystalline Cu(111) films were prepared on sapphire(0001) substrates by DC sputtering and post-deposition annealing. The graphene layer was then transferred onto a 50 nm thick $SiO_2$ layer on Si(100) substrate [18]. The structure of the graphene layer was determined to be single crystal through azimuthal RHEED reciprocal space mapping [24].

### 2.2. SnS film preparation

According to the vapor phase diagram, the SnS evaporates congruently during deposition by thermal evaporation [25]. This makes thermal evaporation a desirable method to grow SnS thin film. The advantage of using thermal evaporation of SnS is that thermal evaporation introduces negligible disorder in the single layer graphene as compared with other deposition techniques such as sputtering, e-beam, and pulsed laser depositions as shown by Raman spectra [26]. The SnS film was grown on graphene/$SiO_2$/Si(100) substrate by evaporating SnS powder (Sigma Aldrich, purity $\geq$ 99.99%) placed in an alumina coated tungsten basket with the top opening diameter of about 1 cm (R.D. Mathis). The substrate was mounted about 15 cm above the SnS source. The base pressure of the vacuum chamber was 5–7 × 10$^{-7}$ Torr. Before a deposition, the substrate was heated to 280 °C from the backside with a ramping rate of 20 °C/min using a double ended halogen lamp (Ushio, FCL, J120V-500 W) with a rectangular reflector (8 cm × 12 cm) installed inside the vacuum chamber. A schematic of the experimental setup of the thermal evaporator is shown in Fig. 1(a). During the deposition, the temperature of the substrate surface was maintained at 283–286 °C, which was monitored using a type K thermocouple attached to the substrate surface. The deposition rate was about 0.6–0.8 Å/s according to a quartz crystal monitor (QCM) with a gold coated quartz monitor crystal (Inficon, 008-010-G10). After the deposition, the lamp was turned off immediately. The substrate and the deposited SnS film were cooled down naturally. Both SnS films of about 500 nm thickness were deposited simultaneously on the polycrystalline and single crystal graphene substrates using this system. Fig. 1(b) shows a schematic of the layered structure of the SnS on graphene/$SiO_2$/Si(100) sample.

### 2.3. Characterization techniques used

The surface morphologies of the synthesized SnS films were imaged using an AFM (PSI XE100) in contact mode and a field emission scanning electron microscope (SEM) (ZEISS SUPRA 55). The AFM tip ($\mu$mash, HQ: CSC17/AL BS) used had a tip radius of 8 nm, a force constant of 0.18 N/m, and a resonant frequency of 13 kHz. To characterize the crystal structure and the average grain size of the SnS films in the vertical direction, X-ray diffraction (XRD) was carried out using an X-ray diffractometer (Bruker D8 Discover). The Cu K$\alpha$ X-ray source used had a wavelength of 1.5405 Å. A point detector with a 0.01° scanning step size and a 0.1 s counting time at each step was used to collect the X-ray diffraction theta-2theta ($\theta$-$2\theta$) scans. The scanning step size for the rocking curve was 0.002°. The incident beam, detector, and anti-scatter slits used all had a 0.6 mm width. XRD pole figure measurements were carried out using the same X-ray diffractometer with a 1° step size in both azimuthal and chi directions.
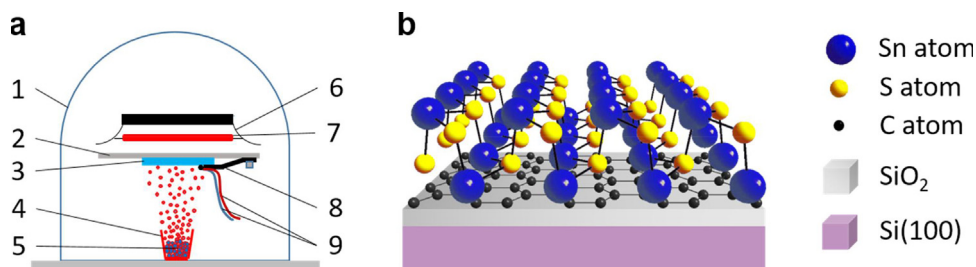
**Fig. 1.** (a) A schematic of the thermal evaporator setup. Major components are labeled by numbers. 1. Glass chamber wall, 2. Substrate holder, 3. Substrate, 4. Alumina coated tungsten basket, 5.SnS powder source, 6. Light reflector, 7. Halogen lamp, 8. Substrate clamp, 9. Thermocouple wires, (b) A schematic of SnS layer on graphene/SiO₂/Si(100) substrate.

The electron backscatter diffraction (EBSD) characterization of SnS films on graphene samples was carried out with a Karl Zeiss Ultra 1540 EsB SEM-FIB system integrated with a NordlysNano EBSD Detector (Oxford Instruments). A 15 kV electron beam was used to scan the sample surface with an area of 5.0 μm × 5.0 μm, a working distance of 18 mm, and a sample tilting angle of 70°. The scanning step size was set at 125 nm. The crystallographic orientation data was collected using the Aztec 2.1 EBSD data acquisition software and post-analyzed using the HKL Channel 5 Mambo software (Oxford Instruments) for the crystallographic orientation mapping, the grain boundary misorientation estimation, and the pole figure plotting.

Reflection high-energy electron diffraction (RHEED) was used to characterize the structure and texture near the surface of the SnS film. The base pressure of the vacuum chamber that housed the RHEED was in the range of $10^{-8}$ Torr. The electron gun (model RDA-003G) used in RHEED generated a 15 keV electron beam incident at a glancing angle of ∼1° on the sample surface and the emission current was 34 μA. The RHEED pattern was projected on a phosphor screen mounted on a 6-in flange which was about 20 cm away from the sample in the vacuum chamber and was captured by a digital camera positioned outside the chamber [27]. The RHEED 2D reciprocal space mapping is constructed from 100 RHEED patterns collected at 100 different azimuthal angles with a 1.8° incremental angle and the details are described elsewhere [24].

Raman spectra were collected using a Renishaw 2000A Raman microscope system. The laser wavelength and power used were 785 nm and 2 mW, respectively. The integration time was 10 s and the laser spot size was 5 μm × 20 μm. The step size used in the Raman scattering data collection was 1 cm⁻¹. The resistivity, carrier density and Hall mobility of the SnS film were measured using a homemade van der Pauw setup [28]. The external DC magnetic field can be raised up to 4500 G. Four indium dots were used as electrical contacts near the edges of four corners of the film. The In dots were secured to the surface of each film at ambient temperature (and without annealing) by applying a pressure from the clamps. Our current vs voltage test shows the contacts are Ohmic [29].

## 3. Results and discussions

### 3.1. Surface morphology

#### 3.1.1. SEM

Fig. 2(a) and (b) show the SEM top views of the polycrystalline graphene and single crystal graphene on SiO₂/Si substrate, respectively. Both Fig. 2(a) and (b) show that the major part of the surface is covered by a graphene layer, but there exists grain boundaries (dark curves), wrinkles and bilayer graphene islands. The lateral size of the bilayer island is about 2 μm for both substrates, but the single crystal graphene surface was covered by fewer bilayer

islands than that on the polycrystalline graphene. Fig. 2(c) and (d) show SEM top views of SnS films grown on the polycrystalline and single crystal graphene substrates, respectively. The surfaces of both SnS films show many flakes scattered on a continuous film. The typical size of an individual flake for the SnS film grown on the single crystal graphene (about 400 nm) is larger than the one grown on the polycrystalline graphene (about 250 nm). Literature reports that adsorbates or particles often decorate at graphene grain boundaries [30]. It was predicted that lines of adsorbates and particles are more reactive than the pristine lattice of graphene. Experimentally we observed that the SnS flakes form clusters along the graphene grain boundaries shown in Fig. 2(a) and (b). This may be due to the fact that these sites are more reactive to initiate the growth of SnS flakes. The number density of SnS flakes on single crystal graphene is lower than that on the polycrystalline graphene, which may be attributed to fewer grain boundaries in the single crystal graphene. Fig. 2(e) and (f) show SEM cross section views of mechanically cleaved SnS films grown on polycrystalline graphene and single crystal graphene substrates, respectively. The thicknesses of the films are ∼527 nm and ∼612 nm in Fig. 2(e) and (f), respectively. The SnS film grown on the polycrystalline graphene has columnar like structure whereas the SnS film grown on the single crystal graphene has large size grains. This large size is supported by the EBSD data to be presented later.

#### 3.1.2. AFM

Fig. 2(g) and (h) show AFM top views of the SnS films grown on polycrystalline graphene and single crystal graphene, respectively. Both films show island-like features over the surface. The high magnification images in the insets of Fig. 2(g) and (h) reveal the details of these features. The root-mean-square roughness of the two surfaces shown in Fig. 2(g) and (h) are ∼37.8 nm and ∼34.3 nm, respectively, which are very comparable. In the literature, typical root-mean-square roughnesses of 500 nm SnS films synthesized through thermal evaporation on various substrates at 300 °C are around 10 nm [31]. Comparing to their results, our SnS films have rougher surfaces. This could be attributed to (1) the surface enengy of SnS(010) (∼154 mJ/m² [32]) is higher than the surface energy of the graphene (∼46.7 mJ/m² at room temperature [33]). Thus SnS does not wet graphene and favors island growth. (2) Low surface diffusion of SnS at the relatively low substrate temperature [34]. Recall that our substrate was held at 280 °C during growth. The film is columnar and grainy. (3) The wrinkles formed (∼10 nm in height) on the initial graphene surface due to graphene's relaxation on SiO₂/Si substrates [35]. The lateral correlation lengths of the surfaces in Fig. 2(g) and (h) are ∼167 nm and ∼286 nm, respectively. This indicates that the distribution of flakes is denser on the polycrystalline graphene than that on the single crystal graphene, which is consistent with the SEM results.
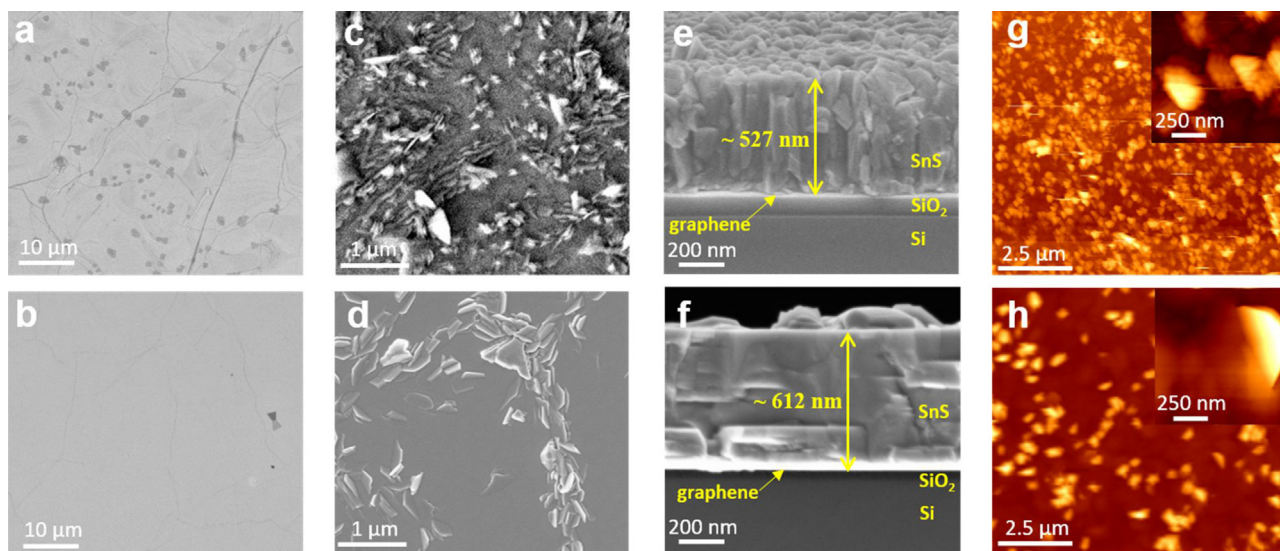
**Fig. 2.** SEM top-view images of (a) bare commercial polycrystalline graphene on SiO$_2$/Si(100), (b) bare homemade single crystal graphene on SiO$_2$/Si(100), (c) after the deposition of SnS film on the polycrystalline graphene, and (d) after the deposition of SnS film on the single crystal graphene. SEM cross-section view images of (e) SnS film on the polycrystalline graphene on SiO$_2$/Si(100) and (f) SnS film grown on the single crystal graphene on SiO$_2$/Si(100). AFM top-view images of (g) SnS film on the polycrystalline graphene and (h) SnS film on the single crystal graphene. The insets in (g) and (h) show zoomed-in views from small areas in (g) and (h), respectively.

### 3.2. EBSD measurements of orientation, grain size and grain boundary orientation

The SnS film on polycrystalline graphene has a rough surface, therefore a significant fraction of the area was unresolved during the EBSD scan. In contrast, a majority of the surface area can be resolved for the smoother SnS film grown on single crystal graphene. The SnS phase is detected to belong to orthorhombic crystal system with a space group of 62 (*Pbnm*). Fig. 3(a) shows the crystallographic orientation map using the inverse pole figure component in the Z-direction (IPF-Z). The uniform blue color map for the SnS film on the single crystal graphene in Fig. 3(a) indicates a homogeneous out-of-plane [010] orientation. Fig. 3(b) shows IPF-X map indicating the in-plane crystallographic orientation distribution in the SnS film. SnS grain boundaries on the single crystal graphene are well resolved in Fig. 3(b). The green color indicates the [001] crystal direction, and the red color indicates the [100] crystal direction. The estimated grain size is about 1 μm for this SnS film. Fig. 3(c) is the grain boundary misorientation histograms for SnS film on single crystal graphene. The plots show that the preferred misorientation angle for SnS film on single crystal graphene are $i \cdot 30°$ where $i$ is an integer.

### 3.3. Analysis of structure and texture by diffraction

#### 3.3.1. X-ray diffraction

Fig. 4(a) and (b) show X-ray diffraction intensity plotted in a logarithmic scale vs $2\theta$ from SnS films grown on the polycrystalline graphene and the single crystal graphene, respectively. For the SnS film shown in Fig. 4(a), SnS(020), (040), (080) peaks at $2\theta$ = 15.72°, 31.87°, and 66.64° as well as Si(400) peak at 69.27° were observed. From these peaks the lattice constant $b$ of SnS is determined to be $11.236 \pm 0.007$ Å (bulk lattice constant $b$ = 11.192 Å). The inset a1 in Fig. 4(a) is a one degree zoomed-in view at the vicinity of the SnS(040) peak plotted in a linear scale showing a SnS(111) peak at 31.64° adjacent to the SnS(040) peak at 31.87°. This implies that the SnS film grown on the polycrystalline graphene may develop more than one crystal orientations. A similar behavior was observed by Devika et al. for the SnS film grown on a glass substrate at 300 °C using thermal evaporation [9]. For the SnS film shown in Fig. 4(b),

SnS(020), (040), (080) peaks at $2\theta$ = 15.80°, 31.91°, and 66.70° as well as Si(400) peak at 69.15° were observed. The lattice constant $b$ of SnS film is determined to be $11.207 \pm 0.008$ Å, closer to the bulk lattice constant $b$. A one degree zoomed-in view plotted in inset b1 shows no SnS(111) peak, unlike the SnS film grown on the polycrystalline graphene. This means that the SnS film grown on the single crystal graphene has a single orientation.

The average vertical coherent domain size D can be estimated from the full-width-at-half-maximum (FWHM) of X-ray peak intensity profile using Scherrer formula $D = K\lambda/(\beta \cdot \cos\theta)$, where $K = 0.89$ is the shape factor, $\lambda$ is the X-ray wavelength, and $\beta$ is the experimental FWHM of the respective ($hkl$) diffraction peak in units of radians. For the SnS film grown on the polycrystalline graphene, the FWHM of the (020) peak is $0.21 \pm 0.01°$. The estimated average vertical coherent domain size is $49.56 \pm 0.02$ nm. Similarly, the estimated average vertical coherent domain size for the SnS film grown on the single crystal graphene is $51.50 \pm 0.02$ nm. These values are smaller than the film thickness observed from SEM and AFM because each morphological feature may consist of many coherent domains. Note that these coherent domain sizes are estimated from measured FWHM without deconvoluting the instrument response's FWHM. Therefore, the sizes are lower limits or underestimated.

Insets a2 and b2 in Fig. 4(a) and (b) show the corresponding rocking curves or omega scans of the SnS(040) peak measured at theta ($\theta$) angle of 15.93° and 15.96° from the SnS films grown on polycrystalline and single crystal graphene, respectively. The FWHMs of rocking curves fitted from the SnS films (without any instrument response deconvolution) by a Gaussian function on the polycrystalline graphene and the single crystal graphene are $0.837 \pm 0.002°$ and $0.860 \pm 0.002°$, respectively. As a reference, the FWHM of the rocking curve measured from the substrate Si(400) peak at $\theta$ angle 34.49° was $0.031 \pm 0.001°$. Our measured FWHMs of around 0.85° are larger than the FWHM of rocking curve of 0.37° observed from SnS film grown on graphene/GaAs(100) or graphene/SiO$_2$/Si but smaller than 2.96° measured from SnS film grown directly on GaAs(100) or ~4° measured from SnS on glass [20]. Note that the reported FWHMs of rocking curves by Wang et al. were measured from ~1 μm thick SnS film grown on bi-layer graphene at 400 °C
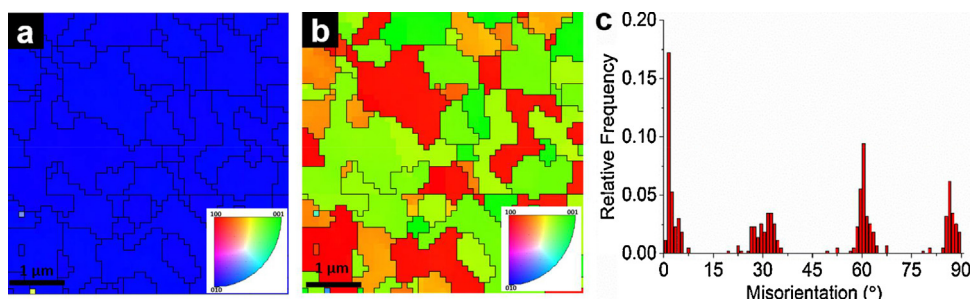
**Fig. 3.** (a) EBSD IPF-Z crystallographic orientation map that shows the out-of-plane orientation in the SnS film on the homemade single crystal graphene. (b) IPF-X map which indicates the in-plane crystallographic orientations and unveils the grain boundaries in the SnS film grown on the single crystal graphene. The scale bars in (a) and (b) are 1 μm. (c) grain boundary misorientation histograms indicating the grain boundary misorientation distributions in the SnS film grown on the single crystal graphene.
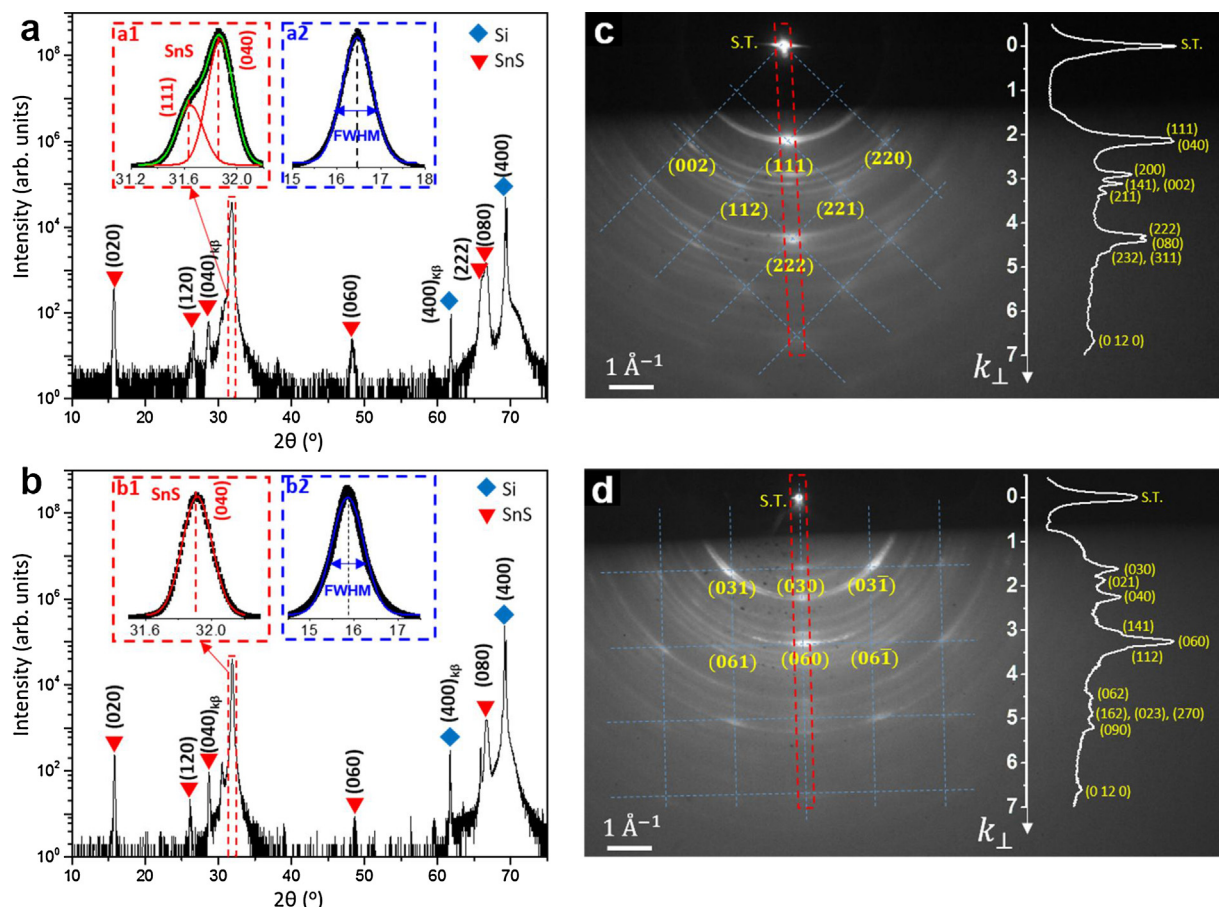


**Fig. 4.** (a) XRD $\theta$ vs $2\theta$ scan from the SnS film deposited on the commercial polycrystalline graphene/SiO$_2$/Si(100) substrate and the intensity is plotted in a logarithmic scale. Inset a1: A zoomed-in view of the XRD $\theta$ vs $2\theta$ scan of the SnS film within the range of 31.2° < $2\theta$ < 32.2° and the intensity is plotted in a linear scale. The profile contains (111) and (040) peaks. Inset a2: The XRD (040) rocking curve of the SnS film with the intensity plotted in a linear scale and 3-degree ω angular range. (b) The XRD $\theta$ vs $2\theta$ scan from the SnS film deposited on the single crystal graphene/SiO$_2$/Si(100) substrate and the intensity is plotted in a logarithmic scale. Inset b1: A zoomed-in view of XRD $\theta$ vs $2\theta$ scan of SnS film within the range of 31.5° < $2\theta$ < 32.5°. and the intensity is plotted in a linear scale. Inset b2: The XRD (040) rocking curve of the SnS film with intensity plotted in a linear scale and 3-degree ω angular range. RHEED pattern using a 15 keV electron beam collected from (c) SnS film grown on the polycrystalline graphene/SiO$_2$/Si(100), and (d) SnS film deposited on the single crystal graphene/SiO$_2$/Si(100) substrates. In each RHEED pattern, (*hkl*) indices were labeled below diffraction spots. The out-of-plane directions in (c) and (d) are [111] and [010], respectively. The diamond and square unit meshes are outlined in blue dashed lines in (c) and (d), respectively. Insets in (c) and (d) show radial intensity vs reciprocal distance or perpendicular momentum transfer k$_\perp$ along the direction perpendicular to the substrate. The red dashed rectangular box in the RHEED pattern indicates the area where the intensity is integrated. The (*hkl*) indices of peaks and rings are labeled (For interpretation of the references to colour in this figure legend, the reader is referred to the web version of this article).

while the thicknesses of our film is only about 500 nm, and our films were grown at 280 °C.

### 3.3.2. X-ray pole figure

The strong (010) out-of-plane orientation and narrow rocking curve of SnS films grown on graphene buffer layers presented above do not reveal the in-plane epitaxy of the SnS film. Fig. 5(a) and

(b) show X-ray {160} pole figures of SnS film on polycrystalline and single crystal graphene, respectively, for the (010) out-of-plane orientation. The $2\theta$ angle for the pole figure measurements was set at 53.443°, and the step size for the azimuthal angle ($\varphi$) and chi angle ($\chi$) scans were both 1°. In the SnS {160} pole figure from the SnS film grown on the polycrystalline graphene shown in Fig. 5(a), 12 almost even intensity poles 30° apart azimuthally at $\chi \sim 23°$

**a**

**b**

**c**

**d**

(10)   (01)   ($\bar{1}$1)   ($\bar{1}$0)   (0$\bar{1}$)   (1$\bar{1}$)

Intensity (arb. units)

$\varphi$ (°)

**e**

$<2\bar{1}\bar{1}0>$
$<01\bar{1}0>$
$<100>$
$<001>$

**f**

$<10\bar{1}0>$
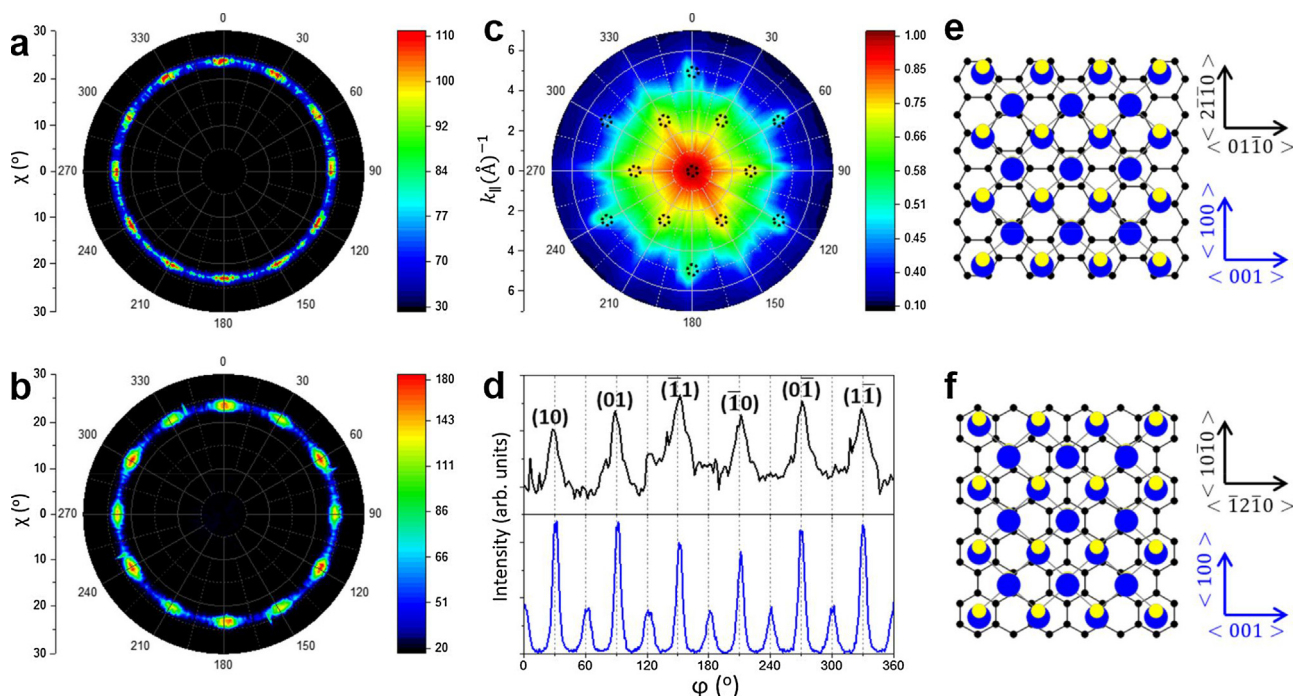$<\bar{1}2\bar{1}0>$
$<100>$
$<001>$

**Fig. 5.** X-ray {160} pole figures with the (010) out-of-plane orientation measured from the SnS films grown on (a) the commercial polycrystalline graphene/SiO$_2$/Si(100) substrate, and (b) the homemade single crystal graphene/SiO$_2$/Si(100) substrate. (c) RHEED 2D reciprocal space structure measured from the single crystal graphene on SiO$_2$/Si(100) substrate. The black dashed circles are the theoretical positions of the reciprocal lattice points of a single crystal graphene. (d) RHEED azimuthal scan (upper curve) from single crystal graphene at $k_\parallel = 2.9\,\text{Å}^{-1}$ and XRD SnS(160) azimuthal scan taken at $2\theta = 53.443°$ and $\chi = 23.311°$. The corresponding (hk) indices of single crystal graphene are labeled above each peak in the RHEED azimuthal scan. Top view of the atomic structure at the SnS/graphene interface showing the epitaxial relationship: (e) $<100>_{\text{SnS}}$ // $<2-1-10>_{\text{graphene}}$ and (f) $<100>_{\text{SnS}}$ // $<10-10>_{\text{graphene}}$. Note that $[10-10]_{\text{graphene}}$ is rotated 30° from $[2-1-10]_{\text{graphene}}$. Carbon, tin and sulfur atoms are represented by black, blue and yellow balls, respectively. Two perpendicular arrows indicate the crystal directions of graphene (black) and SnS (blue) next to each atomic structure (For interpretation of the references to colour in this figure legend, the reader is referred to the web version of this article).

were observed. For the {160} pole figure of SnS film grown on the single crystal graphene shown in Fig. 5(b), there are 12 poles but six out of 12 poles have stronger intensity. The six stronger intensity poles are 60° apart azimuthally and so are the six weaker intensity poles.

### 3.3.3. RHEED 2D reciprocal space mapping

The difference in the pole figures from films deposited on the polycrystalline and single crystal graphene arises from the structural difference between the polycrystalline graphene and single crystal graphene. As was reported in our earlier work [24], commercial polycrystalline graphene exhibits a 12-fold symmetry and the SnS film grown on it will follow the symmetry. That's why the 12 poles of equal intensity were observed. Similar structural characterization using azimuthal RHEED has been performed on the homemade single crystal graphene. Fig. 5(c) shows the 2D reciprocal space structure measured from the single crystal graphene. It is clear that the single crystal graphene has only a 6-fold symmetry, which indicates that the graphene is in the single-crystal form. After the orientation of the single crystal graphene on SiO$_2$/Si substrate was determined, a 500 nm thick SnS film was deposited on it. It is then expected that the SnS film grown on single crystal graphene will also have a 6-fold symmetry.

Fig. 5(d) shows a comparison between RHEED azimuthal scan from the single crystal graphene measured at parallel momentum transfer $(k)_\parallel = 2.9\,\text{Å}^{-1}$ (upper curve) and XRD {160} azimuthal scan from SnS film measured at $2\theta = 53.443°$ (lower curve). The in-plane projection of the SnS(160) plane's normal vector has the same direction as SnS [100]. The azimuthal angle $\varphi = 0°$ was defined as being parallel to graphene [2$\bar{1}\bar{1}$0] direction (the angle between the base vectors of the graphene unit cell is chosen to be 120°) while taking XRD data. RHEED azimuthal scan in

upper curve of Fig. 5(d) has six peaks, corresponding to (10), (01), ($\bar{1}$1), ($\bar{1}$0), (0$\bar{1}$) and (1$\bar{1}$) in the 2D reciprocal space of graphene. In the XRD azimuthal scan from the SnS{160} planes, we expect a 6-fold symmetry. However, there are azimuthally evenly spaced 12 peaks instead of six, and the average separation between two adjacent peaks is $30 \pm 1°$. Among those 12 peaks, six peaks' azimuthal positions align with the six peak positions in the RHEED azimuthal scan from the graphene and the intensities are two to three times higher than the intensities of the six peaks that are 30° apart. This means that although SnS film follows the symmetry of graphene, there exists two sets of domains having preferred relative rotation angles between SnS film and graphene with different probability. Atomic ball models showing 0° and 30° rotation at the interface between SnS(010) lattice and graphene lattice are presented in Fig. 5(e) and (f), respectively. The two perpendicular arrows in black color near each atomic model indicate the in-plane orientation of graphene lattice (black balls) while the arrows in blue indicate that of SnS(010) lattice (blue and yellow balls representing Sn and S atoms, respectively). Majority of the grains in the SnS film follows $<100>_{\text{SnS}}$ // $<10\bar{1}0>_{\text{graphene}}$ epitaxial relationship while the rest follows $<100>_{\text{SnS}}$ // $<2\bar{1}\bar{1}0>_{\text{graphene}}$. Note that the angle between $[10\bar{1}0]$ direction and $[2\bar{1}\bar{1}0]$ direction is 30°. The corresponding rotation angles are ($i\cdot60° + 30°$) and $i\cdot60°$ (where $i$ is an integer). The relative rotation angle is defined as 0° while the SnS [100] direction is aligned with graphene [2$\bar{1}\bar{1}$0] direction. First-principles calculation of the interaction energy for SnS/graphene system has been reported earlier by Leung et al. [15], where they found the surface potential energy between SnS layer and graphene has a global minimum at rotation angle of $i\cdot60°$ and a local minimum at ($i\cdot60° + 30°$). The values of these two angles agree with our experimental results. However, they claimed that $i\cdot60°$ is the

most preferred rotation angle while we found ($i \cdot 60^\circ + 30^\circ$) angles dominates.

Literature reports studies of hetero-systems using graphene as a buffer layer for van der Waals epitaxy. Examples are: (1) Metalorganic chemical vapor deposition of parallel epitaxial CdTe(111) was grown on graphene buffered SiO$_2$/Si [17]. The lattice mismatch between CdTe and graphene is 46% and the symmetry changes from hexagonal graphene to Cubic CdTe. (2) Thermal evaporation of epitaxial CdS(001) film was grown on single crystal graphene buffered SiO$_2$/Si substrate [18]. (3) GaAs film was grown on either exfoliated graphite flakes on Si substrate or CVD graphene on Si substrate. The GaAs film has a good (111) rocking curve of 0.06$^\circ$ but the pole figure show a polycrystalline film [36]. (4) Over 50% of 2D GaSe domains grown on transferred graphene buffer layer on SiO$_2$/Si substrate adopts a preferred orientation with $10.5 \pm 0.3^\circ$ interlayer rotation [37]. This lack of in-plane epitaxy in a film results from the random grain boundaries existed in transferred graphene layer that often has wrinkles [38]. Clear and definite epitaxial film was demonstrated when the graphene layer was grown in situ from SiC wafer. An example is the growth of topological insolating Bi$_2$Se$_3$ film on either graphene buffer layer grown in situ on 4H-SiC wafer substrate [39] or double-layer graphene buffer layer grown in situ on 6H-SiC(0001) substrate [40]. Non-layered epitaxial GaN film with 0.06$^\circ$ rocking curve has also be demonstrated on graphene grown in situ on 4H-SiC(0001) [16]. These previous reports indicate that a transferred graphene buffer layer on an amorphous substrate differs from the graphene layer grown on a single crystal substrate. The structural and grain boundaries of CVD grown graphene on polycrystalline Cu metal foils have relative rotational angles that exist among different grains [41].

### 3.3.4. RHEED patterns

In addition to the 12 poles observed in the X-ray pole figure shown in Fig. 5(a) and (b), there is also a continuous ring at the same chi angle. The ring implies the existence of grains without a preferred in-plane-orientation, which may be associated with the randomly distributed flakes on the flat surface found in the SEM images. To confirm this, we used the surface sensitive RHEED measurement, to characterize the film structure and texture near surface. Fig. 4(c) and (d) show the RHEED patterns of the SnS films grown on the polycrystalline graphene and the singe crystal graphene taken at certain sample's in-plane azimuthal angles. The pattern consists of closely spaced concentric rings of intensity centered on the straight-through (S.T.) spot as well as some localized diffraction intensities at certain positions on each ring. Those rings in RHEED pattern indicate the presence of randomly distributed grains near the surface of the SnS film. Similar RHEED patterns were observed at other in-plane azimuthal angles. The fact that the intensities in the rings are not uniform indicates that the grain orientations near the surface of the SnS films have a texture consisted of grains that are not completely random in all directions [42].

Quantitative analyses of RHEED patterns in the radial direction are presented in the following to obtain the structure near the surface. The corresponding radial scans are inserted on the right in Fig. 4(c) and (d) to show the intensity variation as a function of reciprocal distance or as a function of momentum transfer perpendicular to the substrate ($k_\perp$) for SnS films grown on polycrystalline graphene and single crystal graphene, respectively. These curves were obtained by integrating intensity between the red dashed lines perpendicular to the substrate in the RHEED patterns shown in Fig. 4(c) and (d). Each peak in the radial scans corresponds to a diffraction ring in the RHEED pattern. The shape of each peak is fitted using a Gaussian function after subtracting the background, which is taken to be the diffraction intensity slightly outside of the ring [27]. We took the center of the fitted Gaus-

sian function as the peak position. Setting the straight-through spot as the origin, we can determine the radii of each ring, or namely, the reciprocal distance from the origin to a point on a certain ring, as its corresponding peak position in the radial scan. The reciprocal distance (k) is related to the lattice constants of an orthorhombic crystal through the relation: $k^2 = \frac{4\pi^2}{d_{hkl}^2} = 4\pi^2 \left( \frac{h^2}{a^2} + \frac{k^2}{b^2} + \frac{l^2}{c^2} \right)$. The lattice constants of SnS determined from the XRD are: $a$ = 4.33 Å, $b$ = 11.19Å, $c$ = 3.98 Å. Using these values, we calculated the expected radii of rings associated with different ($hkl$) indices for SnS film. By matching calculated radii with the measured positions of peaks (k), we determined the ($hkl$) for each peak, as is labeled at each peak in the radial scan.

Using the same methodology just described, the spots in the RHEED patterns shown in Fig. 4(c) and (d) were indexed. The SnS film grown on the commercial graphene shows an (111) out-of-plane orientation (diamond unit mesh outlined by dashed blue lines) while the SnS film grown on single crystal graphene shows an (010) out-of-plane orientation (square unit mesh outlined by dashed blue lines). Compared to the XRD results, the RHEED results confirmed the (010) orientation near the surface of the SnS film grown on the single crystal graphene and a dominant (111) orientation near the surface of the SnS film grown on the polycrystalline graphene. Due to the strong electron scattering and the near surface protrusions seen in Fig. 2(c)–(f), RHEED can reveal orientation(s) within the electron mean free path (tens nm) near a surface. The radial scan in Fig. 4(c) shows orientations such as (200), (141), (002), and (211), in addition to the (111) out-of-plane orientation from near the surface of SnS on the polycrystalline graphene. Similarly more orientations such as (021), (141), and (112), in addition to the (010) out-of-plane orientation were observed near the surface of the SnS film grown on the single crystal graphene. This means there exist additional minor orientations near the surface that XRD are not able to detect.

### 3.4. Raman spectroscopy

Raman spectroscopy was used to determine the vibrational modes of SnS films and ascertain the chemical stoichiometry of SnS by examining the presence of other phases (SnS$_2$, Sn$_2$S$_3$) that XRD may not be able to detect [43]. Fig. 6(a) and (b) show Raman spectra from the SnS films grown on the polycrystalline and the single crystal graphene substrates, respectively. In every spectrum, five peaks are observed in the range of 50–400 cm$^{-1}$. The board peak between 240 and 340 cm$^{-1}$ was fitted with three Gaussian functions after subtracting a linear background. These fitted peaks' positions are also labeled. All the peak positions of SnS film on the polycrystalline graphene redshift by less than 1 cm$^{-1}$ from those of the counterpart on the single crystal graphene. The peak near 160 cm$^{-1}$ is a B$_{3g}$ vibration mode and the rest three sharp peaks (95, 190, and 219 cm$^{-1}$) and the 1st fitted peak (261 cm$^{-1}$) from the broad peak are identified as A$_g$ vibrational modes. The first four sharp peaks agree with peaks from thin SnS film within 2 cm$^{-1}$ [44]. The 3rd fitted peak at $\sim$310 cm$^{-1}$ from the broad peak may originate from a trace amount of SnS$_2$ [43,45,46] that has only one strong peak ranging from $\sim$312 to 315 cm$^{-1}$. As a reference, the Raman peak measured from a bulk single crystal SnS$_2$ is 315 cm$^{-1}$ [47]. Nine Raman active modes have been observed from single crystal Sn$_2$S$_3$ by Chandrasekhar et al. and the strongest peaks are at $63 \pm 2$ cm$^{-1}$ (A$_g$ mode) and $308 \pm 2$ cm$^{-1}$ (A$_g$ mode) [48]. In our Raman spectra no peak is observed at $\sim$60 cm$^{-1}$ and the peak at $\sim$310 cm$^{-1}$ is weak. We attributed the missing peak at $\sim$60 cm$^{-1}$ to the absence of Sn$_2$S$_3$ and the weak peak at $\sim$310 cm$^{-1}$ to SnS$_2$. Therefore our Raman spectra verified that the chemical stoichiometry of the film is consistent with the vibration modes mainly comes from SnS and a trace
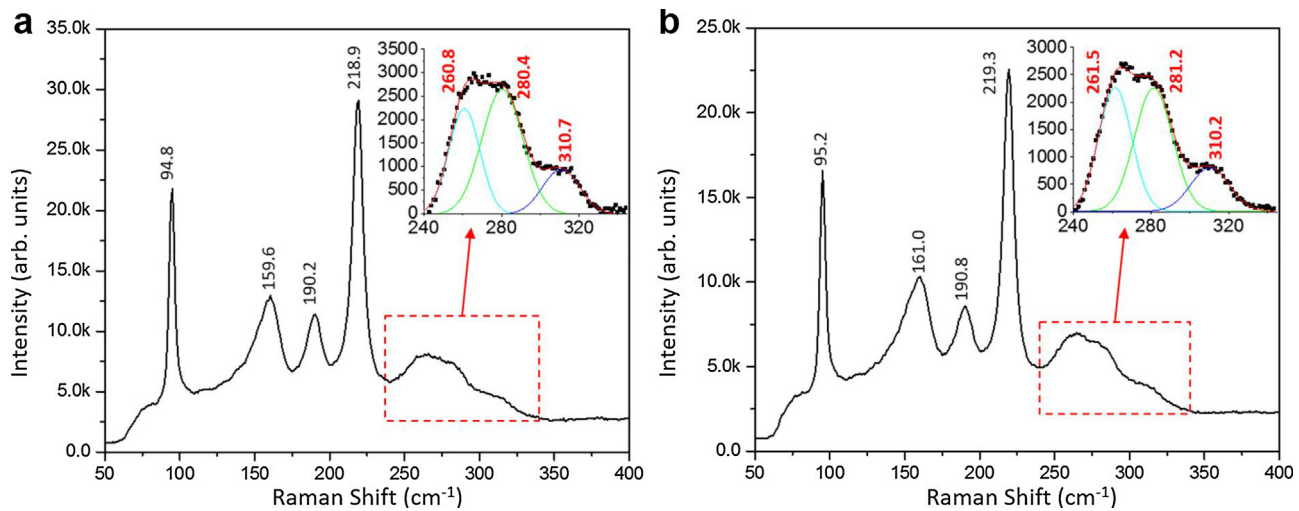
**Fig. 6.** Raman spectra collected at room temperature from the SnS films grown on (a) the commercial polycrystalline graphene and (b) the homemade single crystal graphene. The inset in each figure is the zoomed-in view and Gaussian curve fit of three peaks between 240 and 340 cm$^{-1}$. Peak positions are labeled in each figure.

amount of SnS$_2$. We note the relative intensities between B$_{3g}$ and A$_g$ modes of SnS films reported in the literature vary. Many factors could contribute to this variation, for example, the different crystallographic orientations form in a SnS film from different growth methods. Even for a single SnS phase there is a strong anisotropic Raman response in the measured Raman spectra depending on the incident and scattered light polarization angles [44].

Nikolic et al. [49] has provided approximate estimates of the ratios of the pairs of intra-layer and the inter-layer force constants from the Raman and infrared data. The ratio is about half of that from GeS and GeSe. They infer that although SnS is a layer material the SnS is less layer-like as compared with GeS and GeSe and is intermediate between layer-like and 3D crystal. This may contribute to the growth of islands and flake morphologies that we observed in the SEM and AFM images.

### 3.5. Mobility

Before the Hall mobility measurement of a SnS film, the system was calibrated using a p-type Ge$_{1-x}$Sn$_x$/CaF$_2$(111) sample grown at 350 °C [50]. The room temperature mobility and carrier concentration was repeatedly measured to be $75 \pm 13$ cm$^2$/Vs and $(3.6 \pm 0.6) \times 10^{18}$ cm$^{-3}$, respectively. For the SnS film grown on the single crystal graphene (lateral edge length about 1 cm) on SiO$_2$ substrate, the measured room temperature hole mobility ($\mu$h) and resistivity ($\rho$) have small variations under four different applied currents (1, 5, 10 and 50 $\mu$A) and the average values are $240 \pm 40$ cm$^2$/Vs and $0.31 \pm 0.01$ $\Omega$-cm, respectively. The film is determined to be p-type with an average carrier concentration of $(8.6 \pm 1.5) \times 10^{16}$ cm$^{-3}$. For the SnS film grown on the polycrystalline graphene, measurements of the Hall mobility did not yield a consistent result. This is probably due to the columnar structure as shown in Fig. 2(e).

Published Hall mobility values of p-type SnS films vary widely ranging from tens to hundreds cm$^2$/Vs. The values depend on the growth methods, growth conditions, carrier concentrations, and substrates (graphene buffered single crystal, single crystal, or glass). It is expected that epitaxial SnS film has a higher mobility due to less grain boundary scattering compared with non-epitaxial film. The mobility also depends on the impurity concentration that contributes to ionized impurity scattering, which reduces the mobility. For a fixed conductivity the mobility is inversely proportional to the carrier concentration. We compared several mobility values in tens cm$^2$/Vs from thin SnS films: (1) SnS film grown

by molecular beam epitaxy (MBE) on graphene/GaAs(100) substrates has a Hall mobility up to 81 cm$^2$/Vs for p-type Cu doping of $10^{16}$–$5 \times 10^{17}$ cm$^{-3}$ [20]. (2) SnS film grown on mica by MBE has a hole mobility of 28–46 cm$^2$/Vs with a hole concentration on the order of $10^{17}$ cm$^{-3}$ [51]. (3) Ultrathin SnS nanoplate grown on mica by physical vapor transport has in-plane directional dependent mobility ranging from 20–34 cm$^2$/Vs for $10^{19}$ cm$^{-3}$ doping [52]. (4) SnS films grown on glass by pulse laser deposition of SnS$_x$ target on SiO$_2$ has the highest Hall mobility of 28 cm$^2$/Vs and the carrier densities of $1.5 \times 10^{15}$–$1.8 \times 10^{16}$ cm$^{-3}$ [53]. A couple of groups report mobility in hundreds cm$^2$/Vs: (1) Vapor transport deposition of SnS(010) film on NaCl(100) substrates has a Hall mobility of 385 cm$^2$/Vs for carrier density $10^{17}$ cm$^{-3}$ [54]. (2) Vacuum evaporated SnS (040) film grown on glass at 285 °C growth temperature has a Hall mobility of 400–500 cm$^2$/Vs for carrier density of $10^{14}$ cm$^{-3}$ and resistivity of 13–20 $\Omega$-cm [55].

For SnS single crystal bar of size $2 \times 0.5 \times 0.3$ cm$^3$ made by melting stoichiometric amounts of component materials shows a Hall mobility of 65 cm$^2$/Vs and hole densities of $10^{17}$–$10^{18}$ cm$^{-3}$ at room temperature [56]. The same authors also reported anisotropic mobility in the single crystal SnS. The hole mobility in a plane perpendicular to c axis is ~90 cm$^2$/Vs for charge concentration of $3 \times 10^{17}$ cm$^{-3}$ at room temperature. The Hall mobility in the c axes direction (perpendicular to the SnS layers) is about 5 times smaller than that in the layers perpendicular to the c axes [56]. If a thin film plane is perpendicular to the c-axes then the measured hole mobility tends to have a higher value. This is the case in our SnS(010) film and the SnS(010) [54] and SnS(040) films [55].

### 4. Conclusions

We demonstrate that a sub-micron thick layer metal chalcogenide SnS film can be grown epitaxially on an amorphous substrate buffered by a monolayer single crystal graphene. Our structural characterization through X-ray pole figure shows (1) the SnS films grown on both commercial polycrystalline and homemade single crystal graphene substrates are epitaxial films with the [010]$_{SnS}$//[0001]$_{graphene}$ out-of-plane orientation. (2) For vdWEs growth, the structure of the graphene substrate has an influence on the SnS epi-layer. The SnS film will follow the symmetry of the graphene substrate. Even though the SnS film grown on the single crystal graphene exhibits a 6-fold symmetry, there exists two sets of relative rotation angles ($i$·60º and $i$·60º + 30º) between SnS and graphene while the ($i$·60º + 30º) angles dominate. The in-plane epi-

taxy for the dominant domains follows <100>$_{SnS}$ // <10$\bar{1}$0>$_{graphene}$ while the minor domains follow <100>$_{SnS}$ // <2$\bar{1}\bar{1}$0>$_{graphene}$. (3) EBSD IPF-X maps of SnS(010) films on both graphene substrates reveal the in-plane grain boundaries with grain orientation in 30º increment consistent with X-ray result. The grain size in SnS(010) film grown on single crystal graphene is about 1 μm. (4) The RHEED measurement shows that the near surface texture of the SnS film grown on single crystal graphene is (010) while the near surface texture of SnS film grown on polycrystalline graphene has a mixture of (010) and (111) with more dominant (111). (5) The Raman spectra show that the chemical stoichiometry consistent with the vibration modes mainly comes from SnS and a trace amount of SnS$_2$. (6) The average Hall mobility of the thin SnS(010) film is ~240 cm$^2$/Vs for carrier concentration of ~10$^{17}$ cm$^{-3}$ that is higher than SnS films grown on other single crystal substrates with or without graphene buffered layer. The epitaxial SnS film and its excellent electrical property may improve the efficiency of SnS film-based optoelectronic devices.

## Acknowledgements

## References

[1] P. Sinsermsuksakul, L. Sun, S.W. Lee, H.H. Park, S.B. Kim, C. Yang, R.G. Gordon, Overcoming efficiency limitations of SnS-based solar cells, Adv. Energy Mater. 4 (2014) 1400496.

[2] J.A. Andrade-Arvizu, M. Courel-Piedrahita, O. Vigil-Galán, SnS-Based thin film solar cells: perspectives over the last 25 years, J. Mater. Sci.: Mater. Electron 26 (2015) 4541–4556.

[3] A. Tanusevski, Optical and photoelectric properties of SnS thin films prepared by chemical bath deposition, Semicond. Sci. Technol. 18 (2003) 501.

[4] H. Zhang, C. Hu, X. Wang, Y. Xi, X. Li, Synthesis and photosensitivity of SnS nanobelts, J. Alloys Compd. 513 (2012) 1–5.

[5] F. Lu, J. Yang, R. Li, N. Huo, Y. Li, Z. Wei, J. Li, Gas-Dependent photoresponse of SnS nanoparticles-based photodetectors, J. Mater. Chem. C 3 (2015) 1397–1402.

[6] J. Lu, C. Nan, L. Li, Q. Peng, Y. Li, FlexibleSnS nanobelts: facile synthesis, formation mechanism and application in Li-ion batteries, Nano Res. 6 (2013) 55–64.

[7] R.E. Banai, M.W. Horn, J.R.S. Brownson, A review of tin (II) monosulfide and its potential as a photovoltaic absorber, Sol. Energy Mater. Sol. Cells 150 (2016) 112–129.

[8] H. Nozaki, M. Onoda, M. Sekita, K. Kosuda, T. Wada, Variation of lattice dimensions in epitaxial SnS films on MgO (001), J. Solid State Chem. 178 (2005) 245–252.

[9] M. Devika, N. Koteeswara Reddy, M. Prashantha, K. Ramesh, S. Venkatramana Reddy, Y. Hahn, K. Gunasekhar, The physical properties of SnS films grown on lattice-matched and amorphous substrates, Phys. Status Solidi (A) 207 (2010) 1864–1869.

[10] G.R. Bhimanapati, Z. Lin, V. Meunier, Y. Jung, J. Cha, S. Das, D. Xiao, Y. Son, M.S. Strano, V.R. Cooper, L. Liang, S.G. Louie, E. Ringe, W. Zhou, S.S. Kim, R.R. Naik, B.G. Sumpter, H. Terrones, F. Xia, Y. Wang, J. Zhu, D. Akinwande, N. Alem, J.A. Schuller, R.E. Schaak, M. Terrones, J.A. Robinson, Recent advances in two-dimensional materials beyond graphene, ACS Nano 9 (2015) 11509–11539.

[11] D. Guay, W.M.R. Divigalpitiya, D. Belanger, X.H. Feng, Chemical bonding in restacked single-layer MoS$_2$ by X-ray absorption spectroscopy, Chem. Mater. 6 (1994) 614–619.

[12] A. Koma, Van der Waals epitaxy for highly lattice-mismatched systems, J. Cryst. Growth 201–202 (1999) 236–241.

[13] A. Koma, K. Sunouchi, T. Miyajima, Special issue on nanometer structure electronics fabrication and characterization of heterostructures with subnanometer thickness, Microelectron. Eng. 2 (1984) 129–136.

[14] M.I.B. Utama, Q. Zhang, J. Zhang, Y. Yuan, F.J. Belarre, J. Arbiol, Q. Xiong, Recent developments and future directions in the growth of nanostructures by van der Waals epitaxy, Nanoscale 5 (2013) 3570–3588.

[15] K.K. Leung, W. Wang, H. Shu, Y.Y. Hui, S. Wang, P.W. Fong, F. Ding, S.P. Lau, C.-h. Lam, C. Surya, Theoretical and experimental investigations on the growth of SnS van der Waals epitaxies on graphene buffer layer, Cryst. Growth Des. 13 (2013) 4755–4759.

[16] J. Kim, C. Bayram, H. Park, C.-W. Cheng, C. Dimitrakopoulos, J.A. Ott, K.B. Reuter, S.W. Bedell, D.K. Sadana, Principle of direct van der Waals epitaxy of single-crystalline films on epitaxial graphene, Nat. Commun. 5 (2014), 4836.

[17] D. Mohanty, W. Xie, Y. Wang, Z. Lu, J. Shi, S. Zhang, G.–C. Wang, T.–M. Lu, I.B. Bhat, van der Waals epitaxy of CdTe thin film on graphene, Appl. Phys. Lett. 109 (2016) 143109.

[18] X. Sun, Z. Lu, W. Xie, Y. Wang, J. Shi, S. Zhang, M.A. Washington, T.–M. Lu, van der Waals epitaxy of CdS thin films on single-crystalline graphene, Appl. Phys. Lett. 110 (2017) 153104.

[19] M.I. Bakti Utama, Q. Zhang, J. Zhang, Y. Yuan, F.J. Belarre, J. Arbiol, Q. Xiong, Recent developments and future directions in the growth of nanostructures by van der Waals epitaxy, Nanoscale 5 (2013) 3570–3588.

[20] W. Wang, K.K. Leung, W.K. Fong, S.F. Wang, Y.Y. Hui, S.P. Lau, Z. Chen, L.J. Shi, C.B. Cao, C. Surya, Molecular beam epitaxy growth of high quality p-dopedSnS van der Waals epitaxy on a graphene buffer layer, J. Appl. Phys. 111 (2012) 093520.

[21] X. Li, W. Cai, J. An, S. Kim, J. Nah, D. Yang, R. Piner, A. Velamakanni, I. Jung, E. Tutuc, S.K. Banerjee, L. Colombo, R.S. Ruoff, Large-area synthesis of high-quality and uniform graphene films on copper foils, Science 324 (2009) 1312–1314.

[22] X. Liang, B.A. Sperling, I. Calizo, G. Cheng, C.A. Hacker, Q. Zhang, Y. Obeng, K. Yan, H. Peng, Q. Li, Toward clean and crackless transfer of graphene, ACS Nano 5 (2011) 9144–9153.

[23] M. Belyansky, A. Domenicucci, N. Klymko, J. Li, A. Madan, Strain characterization: techniques and applications, Solid State Technol. 52 (2009) 26–29, 31.

[24] Y. Xiang, F.W. Guo, T.–M. Lu, G.–C. Wang, Reflection high-energy electron diffraction measurements of reciprocal space structure of 2D materials, Nanotechnology 27 (2016) 485703.

[25] R. Colin, J. Drowart, Thermodynamic study of tin sulfide and lead sulfide using a mass spectrometer, J. Chem. Phys. 37 (1962) 1120–1125.

[26] X.P. Qiu, Y.J. Shin, J. Niu, N. Kulothungasagaran, G. Kalon, C. Qiu, T. Yu, H. Yang, Disorder-free sputtering method on graphene, AIP Advances 2 (2012) 032121.

[27] J.T. Drotar, T.–M. Lu, G.–C. Wang, Real-time observation of initial stages of copper film growth on silicon oxide using reflection high-energy electron diffraction, J. Appl. Phys. 96 (2004) 7071.

[28] L. van der, PAUW, A method of measuring specific resistivity and Hall effect of discs of arbitrary shape, Philips Res. Rep. 13 (1958) 1–9.

[29] M. Devika, N.K. Reddy, F. Patolsky, K. Gunasekhar, Ohmic contacts to SnS films: selection and estimation of thermal stability, J. Appl. Phys. 104 (2008), 124503-124501-124506.

[30] S. Malola, H. Häkkinen, P. Koskinen, Structural, chemical, and dynamical trends in graphene grain boundaries, Phys. Rev. B 81 (2010) 165447.

[31] M. Devika, N.K. Reddy, K. Ramesh, H. Sumana, K. Gunasekhar, E. Gopal, K.R. Reddy, The effect of substrate surface on the physical properties of SnS films, Semicond. Sci. Technol. 21 (2006) 1495.

[32] V. Stevanović, K. Hartman, R. Jaramillo, S. Ramanathan, T. Buonassisi, P. Graf, Variations of ionization potential and electron affinity as a function of surface orientation: the case of orthorhombic SnS, Appl. Phys. Lett. 104 (2014) 211603.

[33] S. Wang, Y. Zhang, N. Abidi, L. Cabrales, Wettability and surface free energy of graphene films, Langmuir 25 (2009) 11078–11081.

[34] V.R. Minnam Reddy, S. Gedi, C. Park, M. R.W, R.R. K.T, Development of sulphurized SnS thin film solar cells, Curr. Appl. Phys. 15 (2015) 588–598.

[35] Z. Lu, X. Sun, Y. Xiang, M.A. Washington, G.–C. Wang, T.–M. Lu, Revealing the crystalline integrity of wafer-scale graphene on SiO$_2$/Si: an Azimuthal RHEED approach, ACS Appl. Mater. Interfaces (2017) 23081–23091.

[36] Y. Alaskar, S. Arafin, Q. Lin, D. Wickramaratne, J. McKay, A.G. Norman, Z. Zhang, L. Yao, F. Ding, J. Zou, Theoretical and experimental study of highly textured GaAs on silicon using a graphene buffer layer, J. Cryst. Growth 425 (2015) 268–273.

[37] X. Li, L. Basile, B. Huang, C. Ma, J. Lee, I.V. Vlassiouk, A.A. Puretzky, M.-W. Lin, M. Yoon, M. Chi, J.C. Idrobo, C.M. Rouleau, B.G. Sumpter, D.B. Geohegan, K. Xiao, Van der Waals epitaxial growth of two-dimensional single-crystalline GaSe domains on graphene, ACS Nano 9 (2015) 8078–8088.

[38] S. Deng, V. Berry, Wrinkled, rippled and crumpled graphene: an overview of formation mechanism, electronic properties, and applications, Mater. Today 19 (2016) 197–212.

[39] Y. Liu, M. Weinert, L. Li, Spiral growth without dislocations: molecular beam epitaxy of the topological insulator Bi$_2$Se$_3$ on epitaxial Graphene/SiC(0001), PRL 108 (2012) 115501.

[40] C.–L. Song, Y.–L. Wang, Y.–P. Jiang, Y. Zhang, C.–Z. Chang, L. Wang, K. He, X. Chen, J.–F. Jia, Y. Wang, Topological insulator Bi$_2$Se$_3$ thin films grown on double-layer graphene by molecular beam epitaxy, arXiv (2010), preprint arXiv:1007.0809.

[41] P.Y. Huang, C.S. Ruiz-Vargas, A.M. van der Zande, W.S. Whitney, M.P. Levendorf, J.W. Kevek, S. Garg, J.S. Alden, C.J. Hustedt, Y. Zhu, J. Park, P.L. McEuen, D.A. Muller, Grains and grain boundaries in single-layer graphene atomic patchwork quilts, Nature 469 (2011) 389–392.

[42] D. Litvinov, T. O'donnell, R. Clarke, In situ thin-film texture determination, J. Appl. Phys. 85 (1999) 2151–2156.

[43] N. Mathews, H.B. Anaya, M. Cortes-Jacome, C. Angeles-Chavez, J. Toledo-Antonio, Tin sulfide thin films by pulse electrodeposition: structural, morphological, and optical properties, J. Electrochem. Soc. 157 (2010) H337–H341.

[44] J. Xia, X.-Z. Li, X. Huang, N. Mao, D.-D. Zhu, L. Wang, H. Xu, X.-M. Meng, Physical vapor deposition synthesis of two-dimensional orthorhombic SnS flakes with strong angle/temperature-dependent Raman responses, Nanoscale 8 (2016) 2063–2070.

[45] Y.B. Yang, J.K. Dash, Y. Xiang, Y. Wang, J. Shi, P.H. Dinolfo, T.-M. Lu, G.-C. Wang, Tuning the phase and optical properties of ultrathin SnS$_x$ films, J. Phys. Chem. C 120 (2016) 13199–13214.

[46] M.-J. Jeng, H.-C. Yang, L.-B. Chang, Tin sulfide thin films prepared by thermal evaporation and sulfurization, in: 2014 IEEE 40th Photovoltaic Specialist Conference, 2014, pp. 379–381.

[47] A.J. Smith, P.E. Meek, W.Y. Liang, Raman scattering studies of SnS2 and SnSe2, J. Phys. C: Solid State Phys. 10 (1977) 1321–1323.

[48] H. Chandrasekhar, D. Mead, Long-wavelength phonons in mixed-valence semiconductor Sn II Sn IV S3, Phys. Rev. B 19 (1979) 932.

[49] P. Nikolic, P. Mihajlovic, B. Lavrencic, Splitting and coupling of lattice modes in the layer compound SnS, J. Phys. C: Solid State Phys. 10 (1977) L289.

[50] A.J. Littlejohn, T.-M. Lu, L. Zhang, K. Kisslinger, G.-C. Wang, Orientation epitaxy of Ge$_{1-x}$Sn$_x$ films grown on single crystal CaF$_2$ substrates, CrystEngComm 18 (2016) 2757–2769.

[51] S.F. Wang, W.K. Fong, C. Surya, Investigation of low-frequency noise in van der Waals epitaxies, in: 2013 22nd International Conference on Noise and Fluctuations, 2013, pp. 1–4.

[52] Z. Tian, C. Guo, M. Zhao, R. Li, J. Xue, Two-dimensional SnS: a phosphorene analogue with strong in-plane electronic anisotropy, ACS Nano 11 (2017) 2219–2226.

[53] F.-Y. Ran, Z. Xiao, H. Hiramatsu, K. Ide, H. Hosono, T. Kamiya, SnS thin films prepared by H2S-free process and its p-type thin film transistor, AIP Advances 6 (2016) 015112.

[54] A. Wangperawong, S.M. Herron, R.R. Runser, C. Hägglund, J.T. Tanskanen, H.-B.-R. Lee, B.M. Clemens, S.F. Bent, Vapor transport deposition and epitaxy of orthorhombic SnS on glass and NaCl substrates, Appl. Phys. Lett. 103 (2013) 052105.

[55] H. Noguchi, A. Setiyadi, H. Tanamura, T. Nagatomo, O. Omoto, Characterization of vacuum-evaporated tin sulfide film for solar cell materials, Sol. Energy Mater. Sol. Cells 35 (1994) 325–331.

[56] W. Albers, C. Haas, H.J. Vink, J.D. Wasscher, Investigations on SnS, J. Appl. Phys. 32 (1961) 2220–2225.